Liquid-Liquid Phase Transition in Simulated Supercooled Water Nanodroplets

Shahrazad M. A. Malek,[1] Francesco Sciortino,[2] Peter H. Poole,[3] and Ivan Saika-Voivod[4]
[1]Department of Physics, University of the Fraser Valley, Abbotsford, British Columbia V2S 7M7, Canada
[2]Dipartimento di Fisica, Sapienza University of Rome, 00185 Rome, Italy
[3]Department of Physics, St. Francis Xavier University, Antigonish, Nova Scotia B2G 2W5, Canada
[4]Department of Physics and Physical Oceanography, Memorial University of Newfoundland, St. John's, Newfoundland and Labrador A1B 3X7, Canada

(Received 19 September 2024; accepted 4 March 2025; published 31 March 2025)

Using simulations, we demonstrate how a liquid-liquid phase transition (LLPT) manifests in supercooled water nanodroplets. Selecting an interaction potential for which a LLPT occurs in the bulk liquid, we conduct simulations of supercooled water nanodroplets having between 1000 and 80000 molecules. We show that as the droplet size decreases, the Laplace pressure grows large enough to drive the droplets through the transition from the low-density to the high-density liquid phase, and that all droplets in this size range are large enough to have cores exhibiting the structure and properties of bulk water. To guide experiments, we estimate the range of values for the critical pressure of the LLPT in real water that can be observed using nanodroplets, and propose structural and dynamical measures by which the LLPT in nanodroplets can be detected.

DOI: 10.1103/PhysRevLett.134.138001

Despite more than 30 years of effort, experiments to confirm and locate the proposed liquid-liquid phase transition (LLPT) in supercooled water, which separates low-density liquid (LDL) and high-density liquid (HDL) phases, remain challenging [1–7]. This is due primarily to the regime of low temperature $T < 220$ K predicted for the LLPT. At such extreme supercooling, the lifetime of the metastable liquid state prior to the onset of ice formation is on the order of 10 μs in bulk water [6]. An additional complication is that estimates for both the temperature T_c and pressure P_c of the critical point that terminates the LDL-HDL coexistence line depend on the simulation model studied or on the method used to extrapolate experimental data below the homogeneous nucleation temperature [1,2,8–11]. P_c values ranging from 10 to 200 MPa have been proposed, with recent predictions clustered around 100 MPa [12–15].

Recent experiments focus on approaches to address these challenges. For example, Nilsson and coworkers have exploited ultrafast laser pulses to simultaneously heat and pressurize bulk amorphous ice samples to the conditions of the LLPT, which are then probed by femtosecond x-ray laser pulses to capture evidence of the LLPT in the brief time window before the appearance of ice [6,7]. Such experimental results, while significant, are complex to interpret and do not yet provide a complete characterization of the LLPT, including precise estimates for T_c and P_c. Complementary approaches to test for the LLPT are therefore required.

One such approach, which exploits the properties of liquid water nanodroplets, was proposed in Ref. [16]. The strength of this proposal is that it exploits the characteristics of nanodroplets to avoid the challenges faced in studies of bulk water. The crystal nucleation rate for a sample of supercooled liquid is proportional to the sample volume. As a result, ice nucleation is significantly suppressed in nanodroplets compared to a bulk system at the same degree of supercooling. In addition, the Laplace pressure inside a liquid droplet varies as the inverse of the droplet radius. For nanoscale droplets, the Laplace pressure can be significant, creating the possibility to study the liquid under pressure without the need to impose pressure via external means.

Reference [16] used simulations of the TIP4P/2005 water model [17] to show that the density maximum, a well known anomaly of bulk water, is also observed in nanodroplets as small as a few hundred molecules. Reference [16] also showed that the Laplace pressure inside water nanodroplets can reach 200 MPa, and that indications of the LLPT, previously established to occur in bulk TIP4P/2005 water, are observed in the thermodynamic properties of nanodroplets. For TIP4P/2005, the estimate for P_c is 186 MPa [11]. In Ref. [16], attaining a Laplace pressure of 186 MPa required droplets having a number of molecules N on the order of 100. At such small sizes, surface effects dominate the properties of

nanodroplets, inducing significant deviations from bulk behavior. As a result, a sharp LLPT does not occur in TIP4P/2005 nanodroplets, but rather takes the form of a significantly rounded, continuous crossover in thermodynamic properties. Hence, if real water behaved in the same way as TIP4P/2005, nanodroplets could not be used to demonstrate the existence of the LLPT in bulk water.

However, recent studies suggest that P_c for real water may be significantly lower than in TIP4P/2005 [12–14]. If so, it then becomes important to explore the case in which P_c can be reached in nanodroplets having a bulklike interior. To do so, we choose the WAIL model of water, in which the LLPT has been observed at $P_c = 37$ MPa and $T_c = 210$ K [18,19]. Based on the results of Ref. [16], a Laplace pressure of 37 MPa will occur inside water nanodroplets containing on the order of $N = 10^4$ molecules, a droplet size that provides a better promise of observing bulklike behavior, including a sharp LLPT. In the present work, we reveal the physics of a fully developed LLPT occurring in water nanodroplets.

The model we study, the WAIL potential, is a flexible and polarizable water model that uses parameters based on *ab initio* calculations [20]. We carry out molecular dynamics simulations using Gromacs v5.1.2 and v5.1.4 [21–26]. We model each molecule as D_2O to allow us to use a longer time step of 1 fs, instead of 0.5 fs, as used in Ref. [20]. In order to facilitate comparison with previous work, here we convert all density values to correspond to the molecular weight of H_2O. All our simulations use periodic boundary conditions and are conducted in the constant-(N, V, T) ensemble, where V is the system volume, and where T is constrained using the Nosé-Hoover thermostat [27,28]. Long-range electrostatic contributions are evaluated using the Particle-Mesh Ewald method [29]. Further details on our methods are given in Supplemental Material (SM) [30].

Our runs simulate droplets of N molecules in a cubic simulation box with edge length L that is much larger than the expected droplet diameter. We are primarily interested in testing for bulklike properties occurring in the core of water droplets. To quantify the density of the liquid in the droplet core, we define $\rho_{\text{core}} = mN_c/V_c$, where N_c is the number of O atoms within r_c of the droplet center, m is the mass of a water molecule, and $V_c = (4/3)\pi r_c^3$. The value of r_c is chosen to be approximately one-half the droplet radius and is tabulated in Table S1.

Our simulations start from configurations created in three different ways. We use *de novo* (DN) configurations generated from random arrangements of molecules. We also create initial configurations at two different densities by carving out smaller droplets from the interior of our largest ($N = 80000$) droplet during simulations at two temperatures, 210 and 230 K. "Initially low density" (ILD) droplet configurations with $\rho_{\text{core}} = 0.926$ g/cm^3 are obtained from the 210 K run; "initially high density" (IHD) configurations with $\rho_{\text{core}} = 1.025$ g/cm^3 are obtained from the 230 K run. All results presented here are from runs conducted at 210 K (the estimated value of T_c for the WAIL model) initiated from one of these three types of configurations. Details for each run are provided in Table S1.

We monitor equilibration of our droplets from the time dependence of ρ_{core}, shown for each run in Fig. S1. We also evaluate a neighbor correlation function $f(t)$ defined as the fraction of nearest neighbors that remain so over a time t [16]; see SM [30] for details. We fit a stretched exponential function to the decay of $f(t)$ to obtain a relaxation time τ for successive time windows. As shown in Fig. S2, all our runs are much longer than the largest τ observed during the run. Despite this, the variation of ρ_{core} and τ with time shows that several of our runs, particularly for the largest droplets, do not attain a stationary state on the time scale of our simulations. Assuming a monotonic decay to equilibrium, we use these runs to place a bound on the equilibrium value of ρ_{core} and τ.

We define the droplet density profile $\rho(r)$ as the density of molecules that have O atoms in a shell of radius r, as measured from the droplet center of mass evaluated using O atoms only. Density profiles at 210 K for droplets of three sizes are shown in Fig. 1(a). As noted in previous work on cold and supercooled water nanodroplets, we observe that the density near the droplet surface is higher than in the interior [16]. This effect is more pronounced for larger droplets at lower T for the following reasons. The core of a sufficiently large droplet will have bulklike properties, from which deviations are expected approaching the droplet surface. As T decreases below the density maximum of water, the density of the bulklike core will decrease. However, the formation of an open hydrogen bond network is always disrupted near the droplet surface. Therefore, cooling is less effective in lowering the density at the surface compared to the interior, creating a droplet with a denser outer shell surrounding a less dense core.

Figure 2(a) shows our equilibrium estimates for, or bounds on, ρ_{core} as N varies from 1000 to 80000. For our largest droplets, regardless of how they are initiated, ρ_{core} trends toward the predicted value of the bulk density 0.90 g/cm^3 for WAIL water at $T = 210$ K at ambient pressure [19]. As N decreases, a rapid increase in ρ_{core} occurs in a narrow range near a critical value of $N_c \simeq 15000$. For droplets with $N < N_c$, and regardless of how they are initiated, ρ_{core} relaxes at long times to values in the range 1.0 to 1.1 g/cm^3, much higher than the density of the bulk liquid at ambient pressure. This behavior is consistent with a LLPT from LDL to HDL occurring in the droplet core due to the increase in Laplace pressure as droplet size decreases. Significantly, for two runs initiated with ILD configurations, $N = 8963$ and 13697, the behavior of ρ_{core} with time [Fig. S1(b), right panel] suggests that these droplets initially establish a metastable LDL core that subsequently undergoes a phase

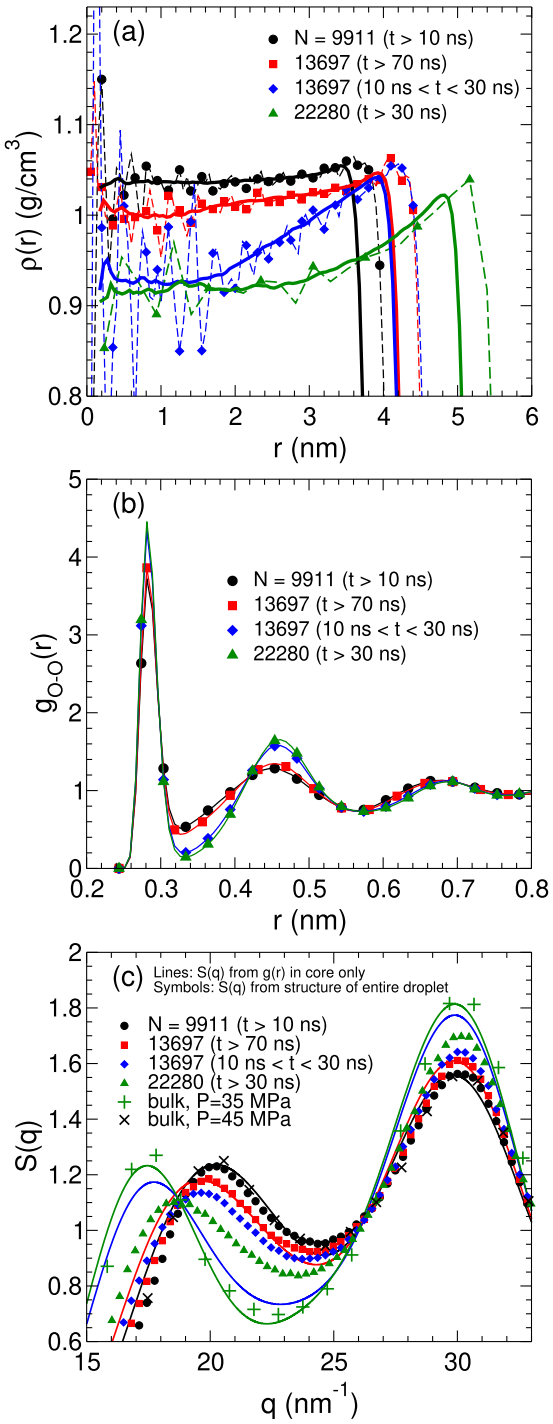

FIG. 1. (a) Density profiles $\rho(r)$ (dashed lines with symbols) for several droplet sizes straddling the LLPT. In each case, the time window for averaging configurations is given. Thick lines show the density profiles evaluated using the Voronoi volumes around each molecule, as described in SM [30]. (b) Radial distribution function $g(r)$ for O atoms in the droplet core. (c) Structure factor $S(q)$ for O atoms. Small symbols show $S(q)$ calculated directly from the positions of all atoms in the droplet. Lines show $S(q)$ evaluated from the $g(r)$ for core O atoms, as described in SM [30]. Large symbols show $S(q)$ from bulk WAIL simulations reported in Ref. [18].

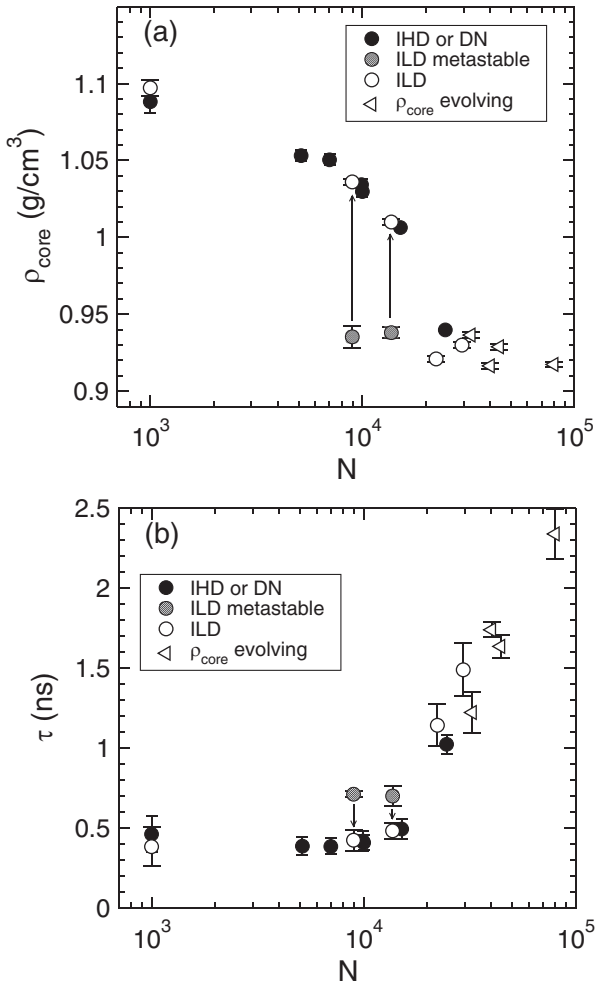

FIG. 2. (a) ρ_{core} and (b) τ versus N at $T = 210$ K. In both panels, circular symbols denote runs in which ρ_{core} is approximately stationary. The time windows for averaging each point are given in Table S1. As described in SM [30], three types of initial configurations are use in these runs: IHD and DN configurations (filled circles) and ILD configurations (open circles). Shaded circles indicate the early time properties of ILD-initiated runs that show evidence of metastability in the form of a low-density state at short time that transforms (see arrows) to a high density state at later time. Triangles locate an upper (lower) bound on ρ_{core} (τ) values for runs that have not reached equilibrium. Error bars are evaluated as described in SM [30].

change to HDL. Such metastability is a hallmark of a first-order phase transition.

Dynamical evidence for the LLPT is shown in Fig. 2(b). As N decreases, the neighbor relaxation time τ decreases and drops sharply in the vicinity of N_c. This behavior is consistent with a phase transition from LDL to HDL as N decreases because bulk LDL is expected to have a significantly larger structural relaxation time than HDL [31]. We again find that the ILD-initiated $N = 8963$ and 13697 runs show evidence of metastability, starting out with a larger τ at early time, corresponding to the LDL

phase, and switching to smaller τ at longer time, when HDL forms.

We next evaluate the pressure inside our droplets to quantify the magnitude of the Laplace pressure corresponding to the density change observed in Fig. 2(a). We define the pressure profile $P(r)$ inside a droplet using the method described in Sec. 3.3 of Ref. [32]; see SM [30] for details. $P(r)$ for a droplet with $N = 1000$ is shown in Fig. S5. As found previously, $P(r)$ is approximately constant in the droplet interior, becomes negative on approach to the surface and then decays to the ambient pressure of the vapor. We define P_{core}, the pressure in the droplet core, by averaging $P(r)$ out to a radius r_{cp} within which we observe $P(r)$ to remain approximately constant. The value of r_{cp} used for each droplet size is recorded in Table S1. Figure 3 plots the values of P_{core} versus ρ_{core} for each of our droplets, compared with the bulk behavior of P versus ρ reported in Ref. [18]. Within the error of our measurements, we find a good correspondence between the droplet and bulk behavior, confirming that the cores of all our droplets are large enough to express bulklike behavior. The value of $P_{\text{core}} \simeq 40$ MPa at which the transition from LDL to HDL occurs in the cores of our droplets is consistent with $P_c = 37$ MPa for the LLPT in bulk WAIL simulations. Note that the data in Fig. 3 show a clear inflection, consistent with the presence of a compressibility maximum as a function of the pressure (at constant T).

The molecular structure in our droplet cores is also consistent with a LDL to HDL transition as N decreases. Figure 1(b) shows the radial distribution function $g(r)$ for O-O pairs where at least one O atom is in the core. We show $g(r)$ for several droplets straddling the phase change, including our $N = 13697$ run which starts in the LDL phase but then switches to the HDL phase. Droplets in the LDL phase show characteristically sharper first and second peaks in $g(r)$ with a deep minimum in between; in the HDL droplets, these features are suppressed. Similarly, Fig. 1(c) shows that the structure factor $S(q)$ for O atoms in our droplet cores compares well with $S(q)$ of the bulk WAIL liquid, both in the LDL and HDL phases [18].

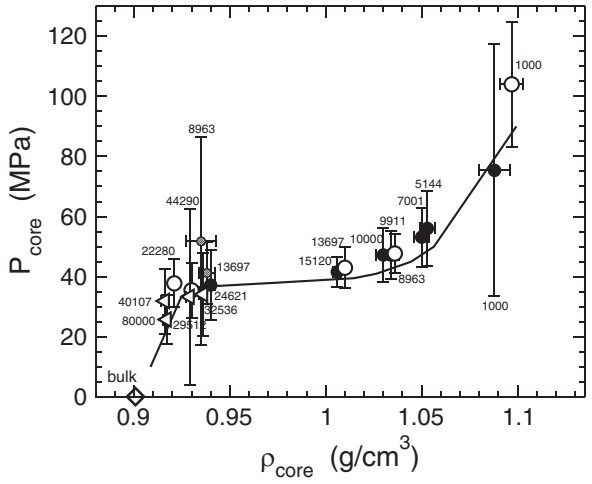

FIG. 3. P_{core} versus ρ_{core} at $T = 210$ K. Nanodroplet size N is indicated for each data point. Symbols have the same meaning as in Fig. 2. The solid curve is the bulk equation of state estimated in Ref. [18]. The diamond indicates the density of the bulk liquid at ambient P evaluated in Ref. [19]. Error bars are ± 2 times the standard error, calculated as described in SM [30].

In summary, our simulations predict that when $P_c = 37$ MPa, the LLPT will occur due to Laplace pressure in nanodroplets at a critical droplet size of $N_c \simeq 15000$. Our results also establish that bulklike behavior occurs in the cores of deeply supercooled water nanodroplets of size $N \gtrsim 1000$. We also find that the Laplace pressure in such droplets reaches as high as 100 MPa. Therefore, if $P_c \lesssim 100$ MPa for the LLPT in real water, then experiments on water nanodroplets in vacuum have the potential to detect the LLPT.

By using the WAIL model, with its low value of P_c, we have shown that a fully developed LLPT can occur in a water nanodroplet. Nonetheless, P_c may be higher than in the WAIL model. For example, $P_c = 90$ MPa for the updated rWAIL model [33] and $P_c = 105$ MPa for the neural network version of the MB-pol model [12]. Using Laplace pressure alone to reach this range of P_c will require the study of small droplets of size $N \sim 1000$, which presents experimental challenges. To address this, we note that the Laplace pressure adds to the pressure of the medium, which in the present work is effectively a vacuum. Investigating nanodroplets surrounded by a pressurizable inert medium may provide a method to tune the pressure in the droplet core to arbitrary values. In this way, much larger droplets, which are easier to produce and more assuredly bulk-like, could be used to test for the LLPT even if $P_c > 100$ MPa.

A range of other experimental approaches could be used to detect the LLPT using nanodroplets. For example: (i) Hyperquenched nanodroplets deposited on a cold surface should produce a low-density aggregate when $N > N_c$, and a high-density aggregate when $N < N_c$. (ii) Experiments that probe the structure of individual droplets, such as those described in Ref. [5], will have to account for the influence of the surface layer of the droplets, which, as we have seen, is not necessarily bulk-like. In Fig. 1(c), we compare the $S(q)$ calculated when only core molecules are considered, and when all the molecules in the droplet are used. When all molecules are used, the characteristic increase in the q value of the first sharp diffraction peak as the system changes from LDL to HDL is still present, but is decreased in magnitude, compared to the $S(q)$ behavior when only core molecules are used. Whether this less dramatic shift can be detected in scattering experiments on nanodroplets will depend on the sensitivity of the measurements. (iii) Estimation of the droplet density, and its variation with N, using the predicted

shape of $S(q)$ at small q for droplets may also be feasible in experiments [34–36]. (iv) The abrupt decrease in the relaxation time of nanodroplets as N decreases can also be an indicator of the LLPT. NMR and dielectric spectroscopy, probing diffusion and rotational dynamics, can provide evidence of a change of behavior on changing N. (v) By using an inert pressure medium as described above, the pressure of a droplet of fixed N could be tuned through P_c. Close to T_c, monitoring the variations in droplet radius may allow for the direct detection of critical fluctuations.

Acknowledgments—We thank the authors of Ref. [18] for providing the data from their simulations shown here in Figs. 1 and 3. We acknowledge useful discussions with P. G. Debenedetti and Barbara Wyslouzil. P. H. P. and I. S.-V. are supported by the Natural Sciences and Engineering Research Council of Canada (NSERC), Grants No. RGPIN-2024-04477 and No. RGPIN-2023-05916, respectively. Computational resources were provided by ACENET (ace-net.ca), a regional partner of the Digital Research Alliance of Canada (alliancecan.ca). F. S. acknowledges support from MIUR-PRIN 2022JWAF7Y, Cineca ISCRAB initiative and ICSC-Centro Nazionale di Ricerca in High Performance Computing, Big Data and Quantum Computing, funded by the European Union "NextGenerationEU".

[1] P. H. Poole, F. Sciortino, U. Essmann, and H. E. Stanley, Phase behaviour of metastable water, Nature (London) **360**, 324 (1992).
[2] O. Mishima and H. E. Stanley, Decompression-induced melting of ice IV and the liquid–liquid transition in water, Nature (London) **392**, 164 (1998).
[3] K. Winkel, E. Mayer, and T. Loerting, Equilibrated high-density amorphous ice and its first-order transition to the low-density form, J. Phys. Chem. B **115**, 14141 (2011).
[4] P. Gallo, K. Amann-Winkel, C. A. Angell, M. A. Anisimov, F. Caupin, C. Chakravarty, E. Lascaris, T. Loerting, A. Z. Panagiotopoulos, J. Russo, J. A. Sellberg, H. E. Stanley, H. Tanaka, C. Vega, L. Xu, and L. G. M. Pettersson, Water: A tale of two liquids, Chem. Rev. **116**, 7463 (2016).
[5] K. H. Kim, A. Späh, H. Pathak, F. Perakis, D. Mariedahl, K. Amann-Winkel, J. A. Sellberg, J. H. Lee, S. Kim, J. Park, K. H. Nam, T. Katayama, and A. Nilsson, Maxima in the thermodynamic response and correlation functions of deeply supercooled water, Science **358**, 1589 (2017).
[6] K. H. Kim *et al.*, Experimental observation of the liquid-liquid transition in bulk supercooled water under pressure, Science **370**, 978 (2020).
[7] K. Amann-Winkel, K. H. Kim, N. Giovambattista, M. Ladd-Parada, A. Späh, F. Perakis, H. Pathak, C. Yang, T. Eklund, T. J. Lane, S. You, S. Jeong, J. H. Lee, I. Eom, M. Kim, J. Park, S. H. Chun, P. H. Poole, and A. Nilsson, Liquid-liquid phase separation in supercooled water from ultrafast heating of low-density amorphous ice, Nat. Commun. **14**, 442 (2023).
[8] V. Holten and M. A. Anisimov, Entropy-driven liquid–liquid separation in supercooled water, Sci. Rep. **2**, 713 (2012), 1207.2101.
[9] V. Holten, C. E. Bertrand, M. A. Anisimov, and J. V. Sengers, Thermodynamics of supercooled water, J. Chem. Phys. **136**, 094507 (2012).
[10] F. Caupin and M. A. Anisimov, Thermodynamics of supercooled and stretched water: Unifying two-structure description and liquid-vapor spinodal, J. Chem. Phys. **151**, 034503 (2019).
[11] P. G. Debenedetti, F. Sciortino, and G. H. Zerze, Second critical point in two realistic models of water, Science **369**, 289 (2020).
[12] F. Sciortino, Y. Zhai, S. L. Bore, and F. Paesani, Constraints on the location of the liquid–liquid critical point in water, Nat. Phys. **21**, 480 (2025).
[13] R. Weldon and F. Wang, Water potential from adaptive force matching for ice and liquid with revised dispersion predicts supercooled liquid anomalies in good agreement with two independent experimental fits, J. Phys. Chem. B **128**, 3398 (2024).
[14] O. Mishima and T. Sumita, Equation of state of liquid water written by simple experimental polynomials and the liquid–liquid critical point, J. Phys. Chem. B **127**, 1414 (2023).
[15] J. R. Espinosa, J. L. F. Abascal, L. F. Sedano, E. Sanz, and C. Vega, On the possible locus of the liquid–liquid critical point in real water from studies of supercooled water using the TIP4P/Ice model, J. Chem. Phys. **158** (2023).
[16] S. M. A. Malek, P. H. Poole, and I. Saika-Voivod, Thermodynamic and structural anomalies of water nanodroplets, Nat. Commun. **9**, 2402 (2018).
[17] J. L. F. Abascal and C. Vega, A general purpose model for the condensed phases of water: TIP4P/2005, J. Chem. Phys. **123**, 234505 (2005).
[18] J. Weis, F. Sciortino, A. Z. Panagiotopoulos, and P. G. Debenedetti, Liquid–liquid criticality in the wail water model, J. Chem. Phys. **157**, 024502 (2022).
[19] Y. Li, J. Li, and F. Wang, Liquid–liquid transition in supercooled water suggested by microsecond simulations, Proc. Natl. Acad. Sci. U.S.A. **110**, 12209 (2013).
[20] E. R. Pinnick, S. Erramilli, and F. Wang, Predicting the melting temperature of ice-ih with only electronic structure information as input, J. Chem. Phys. **137**, 014510 (2012).
[21] M. J. Abraham, T. Murtola, R. Schulz, S. Páll, J. C. Smith, B. Hess, and E. Lindahl, Gromacs: High performance molecular simulations through multi-level parallelism from laptops to supercomputers, SoftwareX **1**, 19 (2015).
[22] S. Pronk, S. Páll, R. Schulz, P. Larsson, P. Bjelkmar, R. Apostolov, M. R. Shirts, J. C. Smith, P. M. Kasson, D. van der Spoel, B. Hess, and E. Lindahl, GROMACS 4.5: A high-throughput and highly parallel open source molecular simulation toolkit, Bioinformatics **29**, 845 (2013).
[23] B. Hess, C. Kutzner, D. van der Spoel, and E. Lindahl, GROMACS 4: Algorithms for highly efficient, load-balanced, and scalable molecular simulation, J. Chem. Theory Comput. **4**, 435 (2008).
[24] D. van der Spoel, E. Lindahl, B. Hess, G. Groenhof, A. E. Mark, and H. J. C. Berendsen, GROMACS: Fast, flexible, and free, J. Comput. Chem. **26**, 1701 (2005).

[25] E. Lindahl, B. Hess, and D. van der Spoel, GROMACS 3.0: A package for molecular simulation and trajectory analysis, Mol. Model. Annu. **7**, 306 (2001).

[26] H. Berendsen, D. van der Spoel, and R. van Drunen, Gromacs: A message-passing parallel molecular dynamics implementation, Comput. Phys. Commun. **91**, 43 (1995).

[27] S. Nosé, A molecular dynamics method for simulations in the canonical ensemble, Mol. Phys. **52**, 255 (1984).

[28] W. G. Hoover, Canonical dynamics: Equilibrium phase-space distributions, Phys. Rev. A **31**, 1695 (1985).

[29] U. Essmann, L. Perera, M. L. Berkowitz, T. Darden, H. Lee, and L. G. Pedersen, A smooth particle mesh Ewald method, J. Chem. Phys. **103**, 8577 (1995).

[30] See Supplemental Material at http://link.aps.org/supplemental/10.1103/PhysRevLett.134.138001 for additional simulation details, analysis and results.

[31] P. H. Poole, S. R. Becker, F. Sciortino, and F. W. Starr, Dynamical behavior near a liquid–liquid phase transition in simulations of supercooled water, J. Phys. Chem. B **115**, 14176 (2011).

[32] S. M. A. Malek, F. Sciortino, P. H. Poole, and I. Saika-Voivod, Evaluating the Laplace pressure of water nanodroplets from simulations, J. Phys. Condens. Matter **30**, 144005 (2018).

[33] R. Weldon and F. Wang, Water potential from adaptive force matching for ice and liquid with revised dispersion predicts supercooled liquid anomalies in good agreement with two independent experimental fits, J. Phys. Chem. B **128**, 3398 (2024).

[34] A. Manka, H. Pathak, S. Tanimura, J. Wölk, R. Strey, and B. E. Wyslouzil, Freezing water in no-man's land, Phys. Chem. Chem. Phys. **14**, 4505 (2012).

[35] A. J. Amaya, H. Pathak, V. P. Modak, H. Laksmono, N. D. Loh, J. A. Sellberg, R. G. Sierra, T. A. McQueen, M. J. Hayes, G. J. Williams, M. Messerschmidt, S. Boutet, M. J. Bogan, A. Nilsson, C. A. Stan, and B. E. Wyslouzil, How cubic can ice be?, J. Phys. Chem. Lett. **8**, 3216 (2017).

[36] A. J. Amaya and B. E. Wyslouzil, Ice nucleation rates near ~225 K, J. Chem. Phys. **148**, 084501 (2018).

SUPPLEMENTAL MATERIAL
Liquid-liquid phase transition in simulated supercooled water nanodroplets

Shahrazad M. A. Malek,[1] Francesco Sciortino,[2] Peter H. Poole,[3] and Ivan Saika-Voivod[4]

[1] *Department of Physics, University of the Fraser Valley, Abbotsford, British Columbia V2S 7M7, Canada*
[2] *Dipartimento di Fisica, Sapienza University of Rome, 00185 Rome, Italy*
[3] *Department of Physics, St. Francis Xavier University, Antigonish, Nova Scotia B2G 2W5, Canada*
[4] *Department of Physics and Physical Oceanography, Memorial University of Newfoundland, St. John's, Newfoundland and Labrador A1B 3X7, Canada*

(Dated: December 10, 2024)

S1. METHODS

We carry out molecular dynamics simulations of water nanodroplets using the WAIL interaction potential and GROMACS v5.1.2 and 5.1.4 [1–6]. We employ a cutoff of 0.9 nm for van der Waals interactions and short-range Coulombic interactions. Long-range electrostatic contributions are evaluated using the Particle-Mesh Ewald method with 6th-order interpolation. All simulations use periodic boundary conditions and are conducted in the constant-(N, V, T) ensemble, where N is the number of molecules, V is the system volume and T is the temperature. Temperature is constrained using the Nosé-Hoover thermostat with $\tau_T = 1.0133$ ps.

De novo (DN) initial configurations are prepared by creating a simulation of N molecules in a cubic simulation box and equilibrating at $T = 300$ K for 500 ps. The edge length L is then increased to a value much larger than the expected droplet diameter. Surface tension quickly transforms the starting cubic liquid droplet in vacuum into a spherical one. This system is then equilibrated at $T = 300$ K for an additional 1 ns. In this time interval, evaporation at this temperature is limited to very few molecules. Then T is lowered to initiate runs at 210 K.

We also create droplet configurations with distinct densities to test how the initial density affects the run. At 230 K, our $N = 80\,000$ droplet has a core density of 1.025 g/cm^3, similar to the bulk high-density liquid (HDL). At 210 K, the core density is 0.926 g/cm^3, similar to the low-density liquid (LDL). To create smaller droplets at each of these densities, we "carve out" droplets of radius R_i from the centre of the $N = 80\,000$ droplets. The runs labelled IHD ("initially high density") in Table S1 are initiated from droplets carved out of the $N = 80\,000$ run at 230 K. Runs labelled ILD ("initially low density") start from droplets carved out of the $N = 80\,000$ run at 210 K.

Table S1 gives the parameter choices for each run, including details on how each is initiated.

S2. VORONOI DENSITY PROFILE

We evaluate the Voronoi density profiles shown in Fig. 1(a) using the method described in Ref. [7]. This alternative way of computing the density profile avoids the fluctuations in $\rho(r)$ that occur because of layering of the molecules in radial shells about the droplet center. In brief, we compute the Voronoi cells for all O atoms. Within each shell of radius r, we compute the total volume $\mathcal{V}(r)$ of the Voronoi cells for O atoms, as well as $\mathcal{N}(r)$, the number of O atoms. We define the average density as determined by the Voronoi cell volumes $\rho_v(r) = m\langle \mathcal{N}(r)/\mathcal{V}(r)\rangle$, where $\langle \cdots \rangle$ indicates an average over the configurations sampled in our simulations, and m is the mass of a water molecule. Note that the Voronoi cells for molecules at the droplet surface have a divergent volume, and so $\rho_v(r)$ vanishes for the outer-most molecular layer.

S3. TIME DEPENDENCE OF THE DENSITY

Fig. S1 shows the time dependence of $\rho_{\rm core}$ in our runs for individual droplets for all droplet sizes. Each run starts from the initial condition specified in Table S1. To test if individual runs are trapped in HDL or LDL-like states due to initial conditions, we run simulations over a wide range of droplet sizes both when starting from IHD and ILD configurations. All runs in Fig. S1(a) are initiated from DN and IHD configurations with an HDL-like density of $\rho_{\rm core} > 0.99$ g/cm^3, while all those in Fig. S1(b) are initiated from ILD configurations with an LDL-like density of $\rho_{\rm core} < 0.94$ g/cm^3.

Many of our runs, especially for larger droplets, do not reach equilibrium on the time scale accessed in our simulations. However, assuming that $\rho_{\rm core}$ and τ vary monotonically with time as the system relaxes to equilibrium, the values of $\rho_{\rm core}$ and τ at late time in these runs provides a bound on the equilibrium density from which qualitative conclusions can be drawn.

The $N = 8963$ and 13697 runs in Fig. S1 appear to flip from a metastable LDL to HDL. On the time scale of our long simulations, we only see a one-way transition, without flipping back to LDL. It is not clear whether flipping will be seen on longer time scales, even if a more precise estimation of N_c is made. In contrast to bulk simulations at constant pressure, for nanodroplets the Laplace pressure changes when the transition occurs. Let us assume that a LDL droplet at P_L transitions to HDL. Since its radius will decrease, the pressure inside will increase to a value $P_H > P_L$. For the LDL droplet to transition to

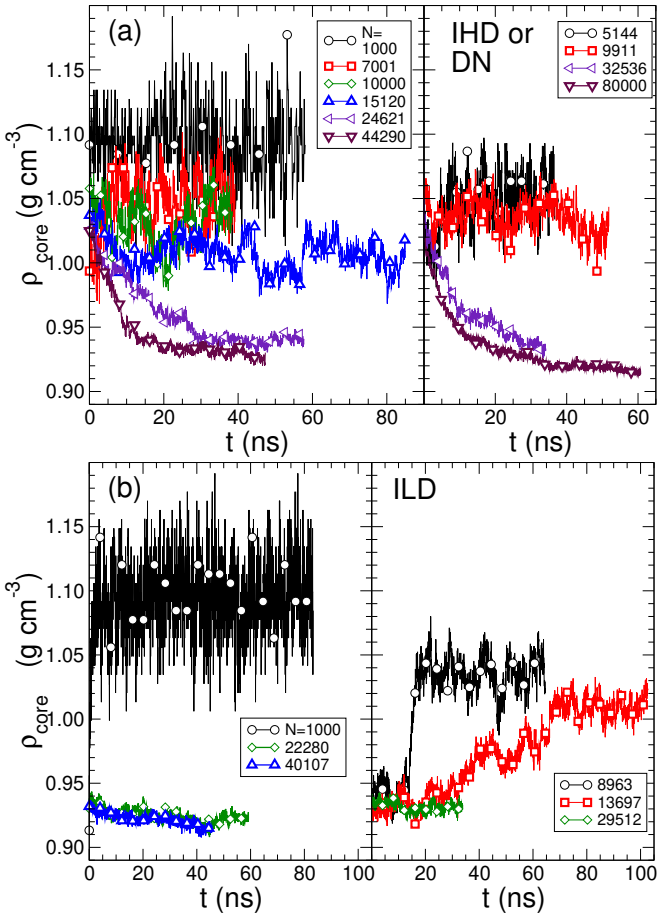

FIG. S1. Time dependence of $\rho_{\rm core}$ for (a) DN and IHD initiated runs and (b) ILD initiated runs.

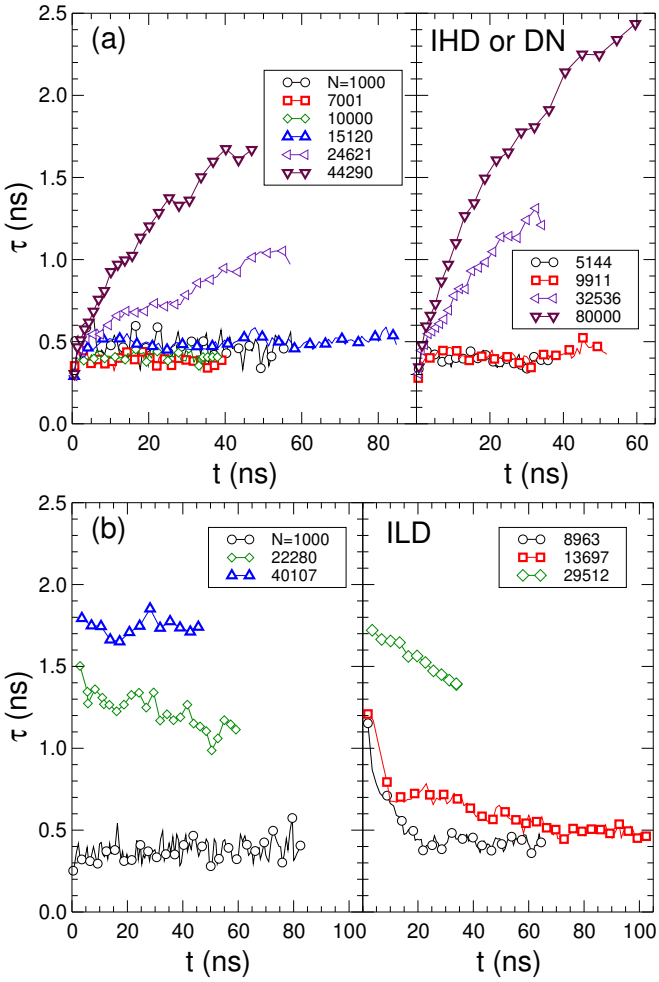

FIG. S2. Time dependence of τ for (a) DN and IHD initiated runs and (b) ILD initiated runs.

HDL, P_L must have been comparable or larger than P_c. Thus after the transition, the HDL droplet is well above P_c, on the HDL branch of the equation of state. At P_H, the barrier to flip back to LDL will be definitively larger than for the initial flip from LDL to HDL. We believe the details of liquid-liquid phase coexistence in nanodroplets merit clarification, which we leave for future work.

S4. RELAXATION TIME

To specify a neighbor correlation function, we define neighbors at $t = t_0$ as two molecules with O atoms separated by less than 0.32 nm. The neighbor correlation function $f(t)$ is the fraction of the original neighbors that remain neighbors after time t. When original neighbours separate by more than 0.32 nm, they are not considered neighbors for all future time. We monitor the decay of $f(t)$ for a fixed time t_{obs} and then compute the relaxation time τ by fitting a stretched exponential function $\exp[(t/\tau)^{\beta}]$ to $f(t)$. t_{obs} is chosen in the range 1 to 3 ns, depending on the average relaxation time of the run. We then reset t_0 to the first time at which $f(t)$ attained a value less than 0.2, and monitor the decay of $f(t)$ in the next time window. In Fig. S2, each value of τ is plotted as a function of the value of $t = t_0$ for each time window.

Fig. S3 shows $f(t)$ in successive time windows for two droplets sizes. For $N = 8963$, we observe that the relaxation process is longer at the beginning of the run than at the end, consistent with the change in the density of this run shown in Fig. S1 from slowly relaxing LDL to more rapidly relaxing HDL. In the case of the $N = 9911$ run, the relaxation time remains approximately constant, and has a smaller value consistent with the HDL phase.

In Fig. S4 we plot τ versus $\rho_{\rm core}$ to clarify how the droplet relaxation time varies with the droplet density.

S5. PRESSURE OF NANODROPLETS

We define the pressure profile $P(r)$ inside a droplet using the method described in Section 3.3 of Ref. [8]. This definition of $P(r)$ is analogous to the thermodynamic ex-

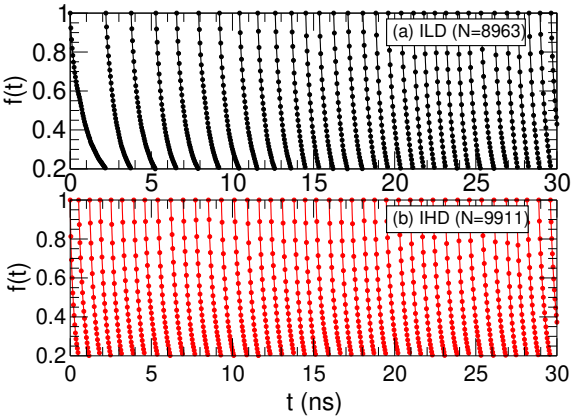

FIG. S3. Neighbour correlation function $f(t)$ for (a) $N = 8963$ (ILD initiated) and (b) 9911 (IHD initiated). Dots are $f(t)$ data while lines are fits of the stretched exponential function $\exp[(t/\tau)^{\beta}]$.

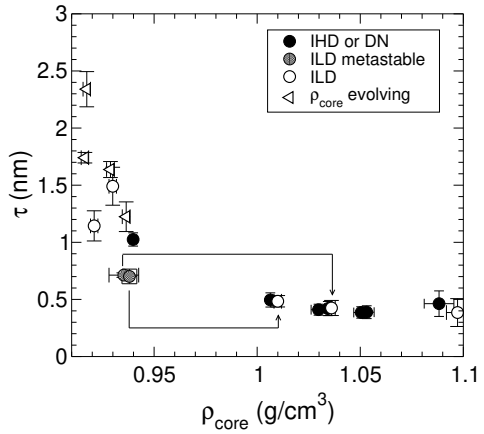

FIG. S4. Relaxation time τ versus $\rho_{\rm core}$. Symbols have the same meaning as in Fig. 2 of the main text.

pression for pressure in a bulk system and is given by,

$$P(r) = \rho(r) k_B T - \left\langle \frac{dU(r)}{dV} \right\rangle_{T,N}, \qquad \text{(S1)}$$

where $U(r)$ is the contribution to the system potential energy of molecules having O atoms in a shell of radius r from the droplet centre of mass to the centre of the shell, k_B is Boltzmann's constant, and $\langle \cdots \rangle$ indicates an average over droplet configurations. When evaluating $U(r)$, the potential energy assigned to each molecule in a shell is half the total binding energy of the molecule with the rest of the system, to avoid double-counting the potential energy of each pair interaction. Ref. [8] showed that estimates of $P(r)$ based on Eq. S1 are within error of those obtained by explicit evaluation of the radial and tangential components of the pressure tensor as a function of r.

To estimate the derivative in Eq. S1, for each configuration we isotropically expand the entire system by a small factor by transforming the position vectors $\mathbf{r}$ of all

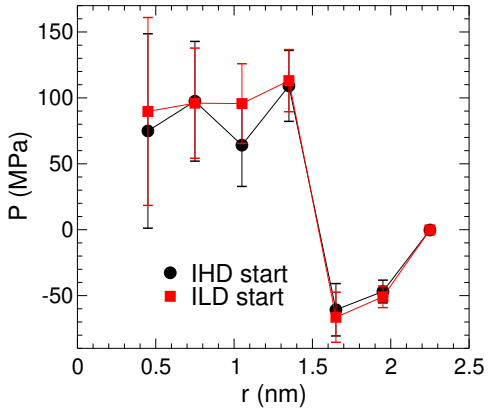

FIG. S5. Pressure profiles $P(r)$ for $N = 1000$ droplets in IHD-initiated and ILD-initiated runs. Error bars are ± 2 times the standard error, calculated as described in section S6.

atoms (i.e. both O and H atoms), relative to the droplet center of mass, according to $\mathbf{r} \to (1+\alpha)\mathbf{r}$, with $\alpha = 10^{-5}$. We find $V(r)$, the volume of each shell of radius r in the unexpanded system, and $V_+(r) = (1+\alpha)^3 V(r)$, the volume that this shell now occupies in the expanded system. Similarly, we find $U(r)$ for each shell in the unexpanded system, and $U_+(r)$, defined as the contribution to the potential energy of the *expanded* system of the same set of molecules located in the shell of radius r in the *unexpanded* system. Note that when calculating contributions to $U(r)$, only interactions between molecules with O atoms separated by less than $r_{\rm cut} = 0.9$ nm are included; no Ewald corrections are applied to account for electrostatic interactions at longer range. When calculating $U_+(r)$, the cut-off distance is increased to $(1+\alpha)r_{\rm cut}$, so that the same set of pair interactions is included in $U_+(r)$ as in $U(r)$. With these definitions, Eq. S1 is approximated by,

$$P(r) = \rho(r) k_B T - \left\langle \frac{U_+(r) - U(r)}{V_+(r) - V(r)} \right\rangle. \qquad \text{(S2)}$$

Fig. S5 shows $P(r)$ for our two $N = 1000$ droplet runs, initiated by IHD and ILD configurations. As found in previous work, $P(r)$ is approximately constant in the droplet interior but upon approaching the surface becomes negative before returning to zero. We define $P_{\rm core}$, the average pressure occurring in the core of a droplet, using

$$P_{\rm core} = \frac{\int_0^{r_{cp}} 4\pi r^2 \, P(r) \, dr}{\int_0^{r_{cp}} 4\pi r^2 \, dr}, \qquad \text{(S3)}$$

where r_{cp} demarcates the distance from the droplet centre of mass over which we observe $P(r)$ to remain approximately constant. The value of r_{cp} used for each droplet size is recorded in Table S1.

The surface tension γ may be estimated using the Laplace equation, $P_{\rm core} = 2\gamma/R$, where R is the droplet radius. We calculate the average radius of gyration R_g

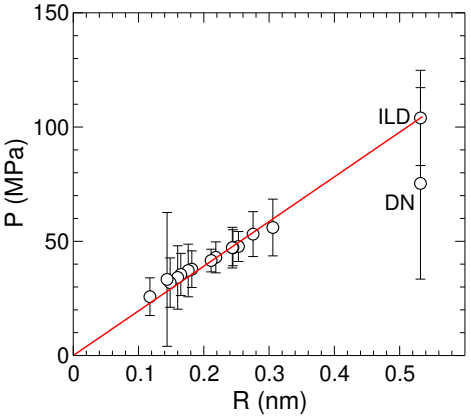

FIG. S6. Core pressure $P_{\rm core}$ of droplets versus the reciprocal of their radius R. The two right-most data points are from the two runs at $N = 1000$, which were initiated differently (DN and ILD). The red line is a linear fit to the data constrained to pass through the origin. The weight of each data point in determining the fit is inversely proportional to the error of each point. Error bars are ± 2 times the standard error, calculated as described in section S6. The surface tension γ is estimated from the slope of the fitted curve.

of each droplet and set $R = \sqrt{5/3} R_g$, as reported in Table S1. Fig. S6 presents our data for $P_{\rm core}$ versus $1/R$, from which γ may be estimated from a fit of a straight line to the data. Fig. S6 shows that our droplets obey the Laplace equation within the error of the data. The obtained value of $\gamma = 97.8 \pm 8.0$ mN/m is higher than the value (85.6 mN/m) predicted by a fit to previous WAIL data obtained at slighly higher T [9].

S6. ERROR BARS

Error bars for $\rho_{\rm core}$ and $P_{\rm core}$ given in Table S1 and displayed in Figs. 2 and 3, and for $P(r)$ displayed in Fig. S5, are $\pm 2\sigma$, where σ is the standard error. For a given quantity x,

$$\sigma = \sqrt{\frac{N'_x}{N_x} \sum_i^{N_x} (x_i - \bar{x})^2}, \tag{S4}$$

where N_x is the number of sample points, and N'_x is the number of independent sample points, determined as the number of successive time windows in the run, each separated by τ in time.

Error bars for τ in Table S1 are twice the standard deviation of τ values between t_i and t_f.

S7. STRUCTURE FACTOR

To calculate the structure factor $S(q)$ from $g(r)$ for O atoms in the droplet core, as shown in Fig. 1(c), we use the general relationship,

$$S(q) = 1 + 4\pi\rho \int_0^\infty r^2 \left[g(r) - 1\right] \frac{\sin qr}{qr}\, dr. \tag{S5}$$

We set $g(r) = 1$ for $r > r_{cg}$ and thus,

$$S(q) = 1 + 4\pi\rho \int_0^{r_{cg}} r^2 \left[g(r) - 1\right] \frac{\sin qr}{qr}\, dr, \tag{S6}$$

where we set $r_{cg} = 1.0$ nm.

[1] M. J. Abraham, T. Murtola, R. Schulz, S. Páll, J. C. Smith, B. Hess, and E. Lindahl, Gromacs: High performance molecular simulations through multi-level parallelism from laptops to supercomputers, SoftwareX **1**, 19–25 (2015).

[2] S. Pronk, S. Páll, R. Schulz, P. Larsson, P. Bjelkmar, R. Apostolov, M. R. Shirts, J. C. Smith, P. M. Kasson, D. van der Spoel, B. Hess, and E. Lindahl, GROMACS 4.5: A high-throughput and highly parallel open source molecular simulation toolkit, Bioinformatics **29**, 845–854 (2013).

[3] B. Hess, C. Kutzner, D. van der Spoel, and E. Lindahl, GROMACS 4: Algorithms for highly efficient, load-balanced, and scalable molecular simulation, J. Chem. Theory Comput. **4**, 435–447 (2008).

[4] D. van der Spoel, E. Lindahl, B. Hess, G. Groenhof, A. E. Mark, and H. J. C. Berendsen, GROMACS: Fast, flexible, and free, J. Comput. Chem. **26**, 1701–1718 (2005).

[5] E. Lindahl, B. Hess, and D. van der Spoel, GROMACS 3.0: A package for molecular simulation and trajectory analysis, Molecular modeling annual **7**, 306–317 (2001).

[6] H. Berendsen, D. van der Spoel, and R. van Drunen, Gromacs: A message-passing parallel molecular dynamics implementation, Comput. Phys. Commun. **91**, 43–56 (1995).

[7] S. M. A. Malek, P. H. Poole, and I. Saika-Voivod, Thermodynamic and structural anomalies of water nanodroplets, Nat. Commun. **9**, 2402 (2018).

[8] S. M. A. Malek, F. Sciortino, P. H. Poole, and I. Saika-Voivod, Evaluating the Laplace pressure of water nanodroplets from simulations, J. Phys. Condens. Matter **30**, 144005 (2018).

[9] R. Weldon and F. Wang, Water Potential from Adaptive Force Matching for Ice and Liquid with Revised Dispersion Predicts Supercooled Liquid Anomalies in Good Agreement with Two Independent Experimental Fits, J. Phys. Chem. B **128**, 3398 (2024).

TABLE S1. Parameters for each run, or segments thereof, used to evaluate the average properties plotted in Figs. 2, 3, S4 and S6. The beginning and end of the time window used to evaluate $\rho_{\rm core}$, $P_{\rm core}$, τ, and R are given respectively by t_i and t_f. $R = \sqrt{5/3}R_g$, where R_g is the radius of gyration. All results are for $T = 210$ K. Runs marked with a triangle provide an upper bound for $\rho_{\rm core}$, the corresponding value of $P_{\rm core}$, and a lower bound for τ.

N	L (nm)	initial config.	R_i (nm)	r_c (nm)	r_{cp} (nm)	t_i (ns)	t_f (ns)	R (nm)	$\rho_{\rm core}$ (g/cm^3)	$P_{\rm core}$ (MPa)	τ (ns)
1000	24	DN	—	1.0	1.4	30	58	1.880 ± 0.0006	1.088 ± 0.007	75.35 ± 41.9	0.463 ± 0.112
1000	45	ILD	1.97	1.0	1.3	30	83.2	1.880 ± 0.0006	1.097 ± 0.005	104 ± 20.84	0.385 ± 0.122
5144	38	DN	—	1.5	2.6	10	36.64	3.270 ± 0.0007	1.053 ± 0.004	56.04 ± 12.42	0.388 ± 0.056
7001	38	DN	—	1.5	3.1	10	39.12	3.630 ± 0.0008	1.05 ± 0.004	53.15 ± 9.82	0.386 ± 0.05
8963	45	ILD	4.10	2.0	3.2	6	9	4.015 ± 0.0017	0.935 ± 0.007	51.78 ± 34.56	0.713 ± 0.02
8963	45	ILD	4.10	2.0	3.2	20	64.48	3.952 ± 0.0009	1.036 ± 0.002	47.72 ± 6.56	0.425 ± 0.066
9911	45	IHD	4.10	1.5	3.2	10	51.8	4.088 ± 0.0008	1.034 ± 0.004	47.19 ± 7.88	0.420 ± 0.062
10000	38	DN	—	2.0	3.4	10	38.36	4.104 ± 0.0013	1.03 ± 0.004	47.23 ± 8.9	0.410 ± 0.048
13697	45	ILD	4.72	2.4	3.8	10	30	4.633 ± 0.0009	0.938 ± 0.004	41.24 ± 10.34	0.701 ± 0.064
13697	45	ILD	4.72	2.4	3.8	70	102.68	4.578 ± 0.0009	1.01 ± 0.002	42.98 ± 6.78	0.484 ± 0.05
15120	45	IHD	4.72	2.4	3.8	20	85	4.735 ± 0.0009	1.006 ± 0.002	41.59 ± 4.96	0.495 ± 0.062
22280	45	ILD	5.55	3.2	4.8	30	59.2	5.506 ± 0.0011	0.921 ± 0.002	37.8 ± 8.02	1.144 ± 0.132
24621	45	IHD	5.55	3.2	4.8	45	57.72	5.678 ± 0.0009	0.94 ± 0.002	37.23 ± 11.52	1.025 ± 0.058
29512	45	ILD	6.09	3.0	5.4	12	33.88	6.069 ± 0.0013	0.93 ± 0.002	35.49 ± 9.24	1.491 ± 0.166
32536$^\triangleleft$	45	IHD	6.09	3.0	5.5	27	34.16	6.250 ± 0.0011	0.936 ± 0.002	34.17 ± 13.88	1.224 ± 0.13
40107$^\triangleleft$	45	ILD	6.75	3.2	6.0	35	45.64	6.736 ± 0.0014	0.916 ± 0.002	31.92 ± 10.8	1.741 ± 0.046
44290$^\triangleleft$	45	IHD	6.75	3.2	6.1	35	47.32	6.960 ± 0.0009	0.929 ± 0.002	33.33 ± 29.28	1.637 ± 0.07
80000$^\triangleleft$	45	DN	—	4.0	7.5	49	60.72	8.514 ± 0.0009	0.917 ± 0.002	25.76 ± 8.24	2.340 ± 0.154